Supporting Information

Engineering built-in electric fields in oxygen-deficient MnO-CeO_2@Cs catalysts: enhanced performance and kinetics for oxygen reduction reaction in aqueous/flexible zinc-air batteries

Lixia Wang [a], Xinran Hu [a], Huatong Li [a], Zhiyang Huang [a], Jia Huang [a], Tayirjan Taylor Isimjan [b,*], and Xiulin Yang [a,*]

[a] *Guangxi Key Laboratory of Low Carbon Energy Materials, School of Chemistry and Pharmaceutical Sciences, Guangxi Normal University, Guilin 541004, China*

[b] *Saudi Arabia Basic Industries Corporation (SABIC) at King Abdullah University of Science and Technology (KAUST), Thuwal 23955-6900, Saudi Arabia*

E-mail: xlyang@gxnu.edu.cn; isimjant@sabic.com

Preparation of catalyst electrode

The catalyst was prepared by dispersing 2 mg of it in a solution containing 200 μL of isopropanol, 100 μL of deionized water, and 5 μL of Nafion. This mixture was then sonicated for 30 minutes to ensure even distribution. Subsequently, 15.68 μL a of this catalyst ink was applied to a rotating disk electrode (RDE) and 19.76 μL to a rotating ring-disk electrode (RRDE), both of which had been previously cleaned. For benchmarking purposes, a commercially available Pt/C was also prepared using an identical procedure.

Materials characterization

Scanning electron microscopy (SEM, Quanta FEG 200, Holland) and transmission electron microscopy (TEM, Talos F200S) were performed to reveal the morphology of catalysts. The X-ray diffraction (XRD) was tested by using Rigaku D/Max-3c with Cu Kα radiation (λ = 0.15418 nm) to character the composition of samples. Raman spectroscopy (Renishaw in Via Quotation) was executed to distinguish the graphitization degree of the catalysts. X-ray photoelectron spectroscopy (XPS, ESCALAB 250Xi) was employed to analyze the elemental and surface valence states of the materials. The work function of the material was analyzed by using ultraviolet photoelectron spectroscopy (UPS, AXIS SUPRA+). The actual metal contents in different catalysts were detected by inductively coupled plasma mass spectrometry (ICP-MS, PekinElmer Corporation, FLexar-NexION300X). The Quantachrome instrument (3H-2000PS4) was utilized to analyze the Brunauer-Emmett-Teller (BET) specific surface area and pore size distribution of the materials. And electron paramagnetic resonance (EPR, Bruker A300) spectroscopy was carried out to measure the relative intensity of oxygen vacancies.

Electrochemical measurements

The ORR activity was measured on an electrochemical workstation (CHI 760E) with a three-electrode system, graphite rod and Ag/AgCl (saturated KCl) electrode as auxiliary and reference electrodes, respectively. The rotating ring disk electrode (RRDE, diameter = 5.61 mm, PINE instruments, USA) and rotating disk electrode (RDE, diameter = 5 mm, PINE instruments, USA) loaded with catalyst ink were used as working electrodes. 2 mg of

electrocatalyst was mixed with 200 μL of isopropanol, 100 μL of deionized water, and 5 μL of 5 wt% Nafion, and then sonicated for 1 h to form a homogeneous catalyst ink. Afterwards, 20 μL of catalyst ink was dropped onto the RRDE surface and allowed to dry naturally in the environment.

The RHE calibration was performed in 0.1 M KOH solution saturated with high purity hydrogen. Two polished Pt plates were used as working and counter electrodes, and an Ag/AgCl electrode was used as reference electrode (Fig. S1). The CV test was performed at a scan rate of 5 mV s^{-1}, and the average potential at zero current was used as the thermodynamic potential for the hydrogen electrode reaction. In 0.1 M KOH, the zero points were 0.9786 V and 0.9425 V, and their average value was 0.961 V. This value was in good agreement with the estimated value of 0.964 V from the Nernst equation. The pH value of the 0.1 M KOH solution was 12.9, so the measured potential was converted to the reversible hydrogen electrode (RHE) by the Nernst equation：

$$E_{RHE} = E_{Ag/AgCl} + 0.059pH + E^{\ominus}_{Ag/AgCl} \quad (1)$$

Cyclic voltammetry (CV) measurements were first performed in O_2/N_2 saturated 0.1 M KOH solution with a potential range of -0.9 ~ 0.2 V versus reference electrode at a scan rate of 30 mV s^{-1}. In addition, linear sweep voltammetry (LSV) curves of different catalysts were obtained in O_2/N_2-saturated 0.1 M KOH electrolyte at a rotation speed of 1600 rpm, and the LSV curves of MnO-CeO_2@Cs catalyst at different rotation rates (400-2025 rpm). The methanol tolerance and long-term stability were measured by chronoamperometry in O_2-saturated 0.1 M KOH at a rotation speed of 1600 rpm. And the Tafel slopes were given by the Tafel equation:

$$\eta = b\, log(\frac{j}{j_0})$$

Based on the LSV results, the electron transfer number (n) is determined according to the following Koutechy-Levich (K-L) equation:

$$\frac{1}{j} = \frac{1}{j_L} + \frac{1}{j_k} = \frac{1}{j_L} + \frac{1}{B\omega^{1/2}}$$

$$B = 0.62nFC_0\nu^{-1/6}{D_0}^{2/3}$$

$$J_K = nFkC_0$$

where J, J_K and J_L represent the actual measured, kinetic, and diffusion-limiting current densities (mA cm^{-2}), respectively. The ω is the angular velocity of the rotating electrode (rad s^{-1}), n is the electron transfer number of oxygen reduction, F is the Faraday constant (F = 96485 C mol^{-1}), C_0 and D_0 are the bulk concentration (1.2×10^{-3} mol L^{-1}) and the diffusion coefficient (1.9×10^{-5} cm^2 s^{-1}) of O_2 in 0.1 M KOH, respectively. The ν is the kinematic viscosity of the electrolyte (0.01 cm^2 s^{-1}), and k is the electron transfer rate constant.

The H_2O_2 yield (%) and actual electron transfer number n during ORR process were calculated based on the RRDE test results combined with the following equation:

$$n = 4\frac{I_d}{I_d + I_r/N}$$

$$H_2O_2\,(\%) = 200\frac{I_r/N}{I_d + I_r/N}$$

I_d and I_r represent the disk and ring currents, respectively, and the collection efficiency of the ring is N = 0.37.

Electrochemical surface area (ECSA) calculation

To measure the electrochemical capacitance, the electrode potential was scanned between 0.12 and 0.24 V (*vs* Ag/AgCl) at different scan rates (4-40 mV s^{-1}). The capacitance in the range of 20-60 mF cm^{-2} is typically observed for flat surface. The electrochemically active surface area was calculated as:

$$A_{ECSA} = \frac{specific\ capacitance}{60\ \mu F\ cm^{-2}_{geo}\ per\ cm^{-2}_{ECSA}}$$

From Fig. S11, ECSA can be calculated for MnO-CeO_2@Cs, MnO@Cs, and CeO_2@Cs.

$$A_{ECSA}(MnO - CeO_2@Cs) = \frac{12.1\ mF\ cm^{-2}}{60\ \mu F\ cm^{-2}_{geo}\ per\ cm^{-2}_{ECSA}} = 201.7\ cm^{2}_{ECSA}$$

$$A_{ECSA}(MnO@Cs) = \frac{11.7\ mF\ cm^{-2}}{60\ \mu F\ cm^{-2}_{geo}\ per\ cm^{-2}_{ECSA}} = 195.0\ cm^{2}_{ECSA}$$

$$A_{ECSA}(CeO_2@Cs) = \frac{2.0\ mF\ cm^{-2}}{60\ \mu F\ cm^{-2}_{geo}\ per\ cm^{-2}_{ECSA}} = 33.3\ cm^{2}_{ECSA}$$

Zn-air batteries (ZAB) fabrication and test

2 mg of catalyst was dispersed in a mixture of 200 μL of ethanol, 200 μL of deionized water, and 5 μL of 5 wt% Nafion and sonicated for 30 min. The resulting mixture was then dropwised on carbon paper (1 cm × 1 cm), dried at room temperature and served as an air cathode. Zinc foil was employed as the anode, and 6.0 M KOH solution containing 0.2 M $Zn(CH_3COO)_2$ was used as the electrolyte.

The polarization curves and open circuit voltage (OCV) of MnO-CeO_2@Cs-based ZAB were obtained using a CHI 760E electrochemical workstation, and stability were tested of the ZAB were conducted using a RAND battery test system (BT2016A) at a current density of 5 mA cm^{-2} for 20 min at each charge/discharge cycle.

The specific capacity was calculated according to the following equation:

$$Specific\ capacity = \frac{discharge\ current \times time}{weight\ of\ consumed\ Zinc}$$

Assembly of flexible solid-state Zn-air batteries (ZAB)

The preparation method of the catalyst ink was the same as that of the Zn-air battery, and the loading of MnO-CeO_2@Cs and Pt/C was 2 mg cm^{-2}. The catalyst coated carbon cloth, zinc foil and polyvinyl alcohol hydrogel (PVA gel) electrolyte served as cathode, anode and solid electrolyte, respectively, and nickel foam was regarded as the current collector to assemble the flexible solid-state zinc air battery. The solid-state electrolyte was synthesized by the following procedure. First, polyvinyl alcohol (PVA, 5 g) was added to 50 mL of deionized water and stirred at 90 °C for 1 h to prepare a gel polymer electrolyte. Subsequently, 5 mL of a mixed solution of 18 M KOH and 0.02 M $Zn(CH_3COO)_2$ was added to the above solution and continued stirring for 30 min. Finally, the resulting paste was frozen at -20 °C to obtain a solid

electrolyte, and thawed at room temperature for further use.

Computational methods:

We performed spin-polarized density functional theory (DFT) calculations using the Vienna ab initio simulation package (VASP) [2, 3]. For the exchange-correlation potential in our calculations, we opted for the Perdew, Burke, and Ernzerhof (PBE) generalized gradient approximation (GGA) [4]. We utilized the projector-augmented-wave (PAW) method to describe the pseudo-potential in our calculations [5]. We iteratively optimized the geometry until the magnitude of the Hellmann-Feynman forces acting on each atom fell below 0.03 eV·Å^{-1}. The iterative solution of the Kohn-Sham equation was terminated when the energy convergence criterion reached 10^{-6} eV.

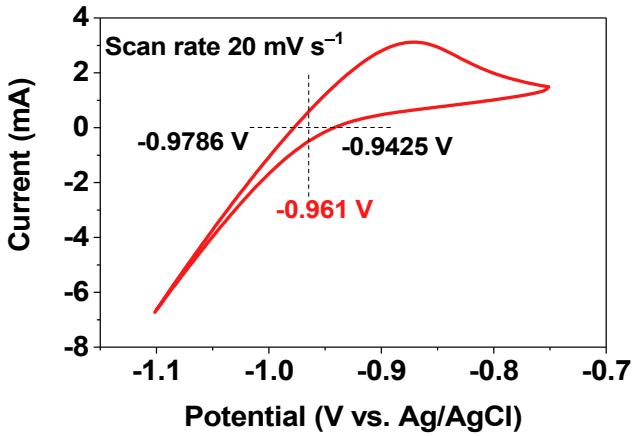

Fig. S1. RHE calibration of saturated Ag/AgCl electrode in 0.1 M KOH.

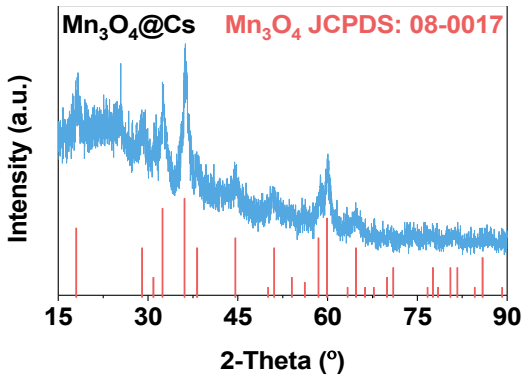

Fig. S2. XRD patterns of precursor Mn_3O_4@Cs.

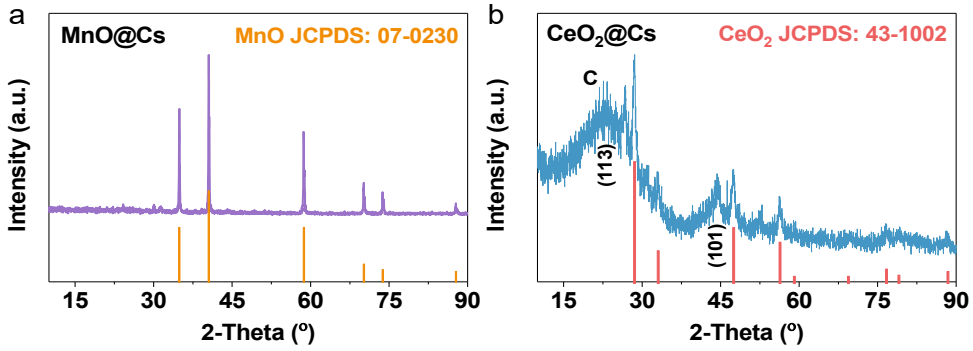

Fig. S3. XRD patterns of (a) MnO@Cs, and (b) CeO_2@Cs.

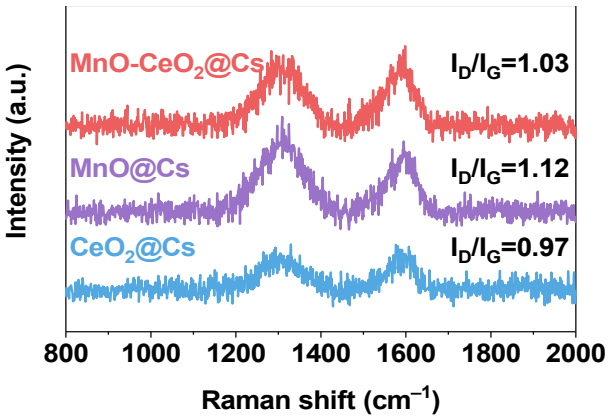

Fig. S4. Raman spectra of the as-prepared MnO-CeO_2@Cs, MnO@Cs, and (c) CeO_2@Cs.

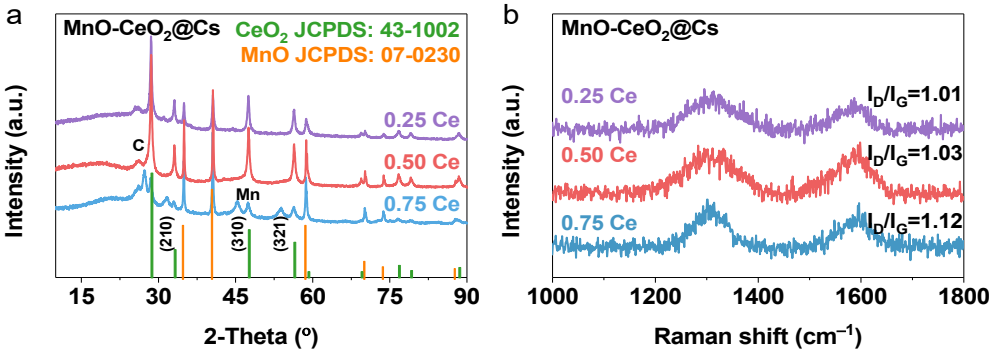

Fig. S5. (a) XRD patterns, and (b) Raman spectra of MnO-CeO_2@Cs with different Ce molar contents.

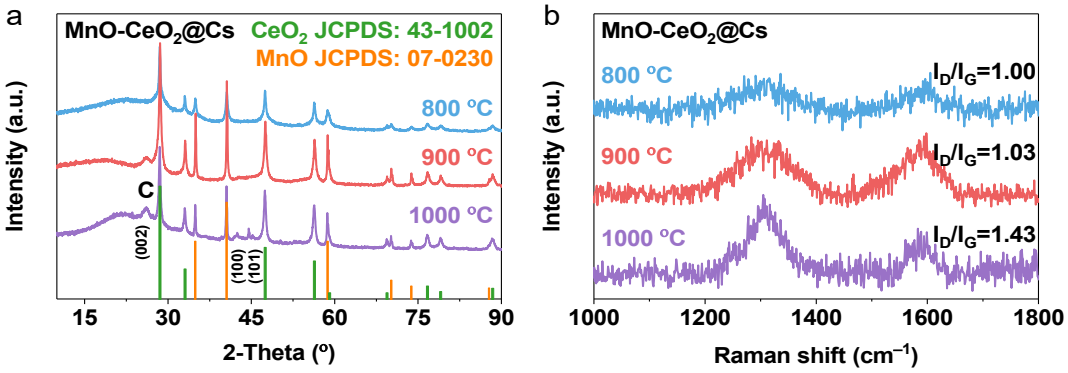

Fig. S6. (a) XRD patterns, and (b) Raman spectra of MnO-CeO_2@Cs at different calcination temperatures.

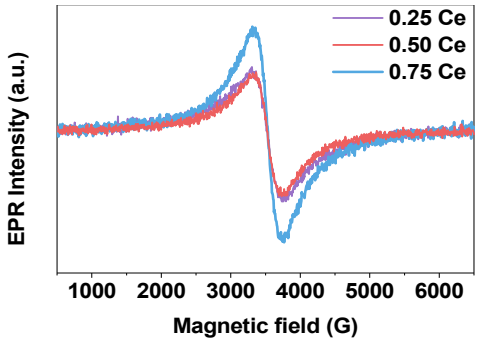

Fig. S7. EPR spectra of MnO-CeO_2@Cs with different Ce molar contents.

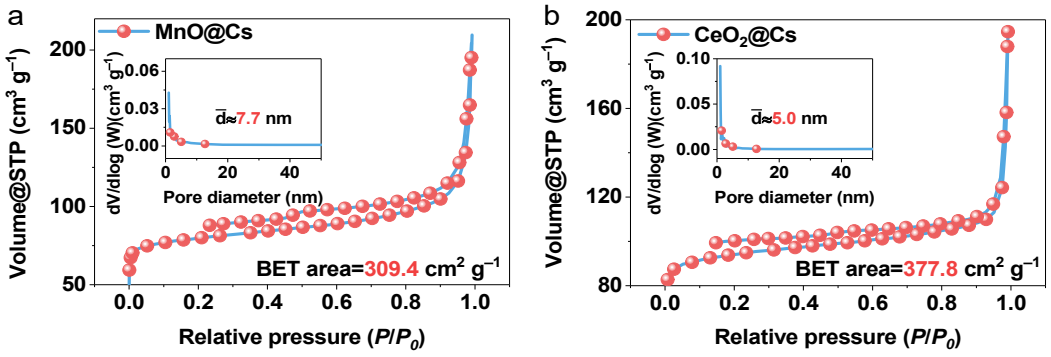

Fig. S8. N_2 adsorption-desorption isotherm of MnO@Cs and CeO_2@Cs.

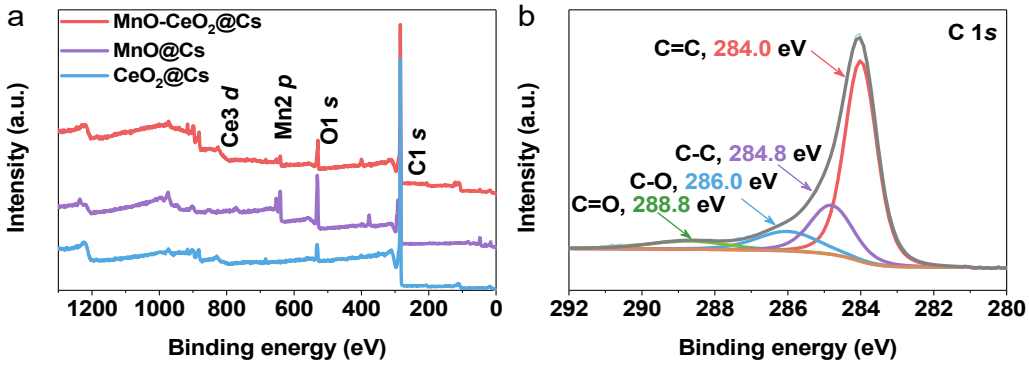

Fig. S9. (a) XPS wide spectra of MnO-CeO_2@Cs, MnO@Cs and CeO_2@Cs. (b) High-resolution XPS spectrum of MnO-CeO_2@Cs.

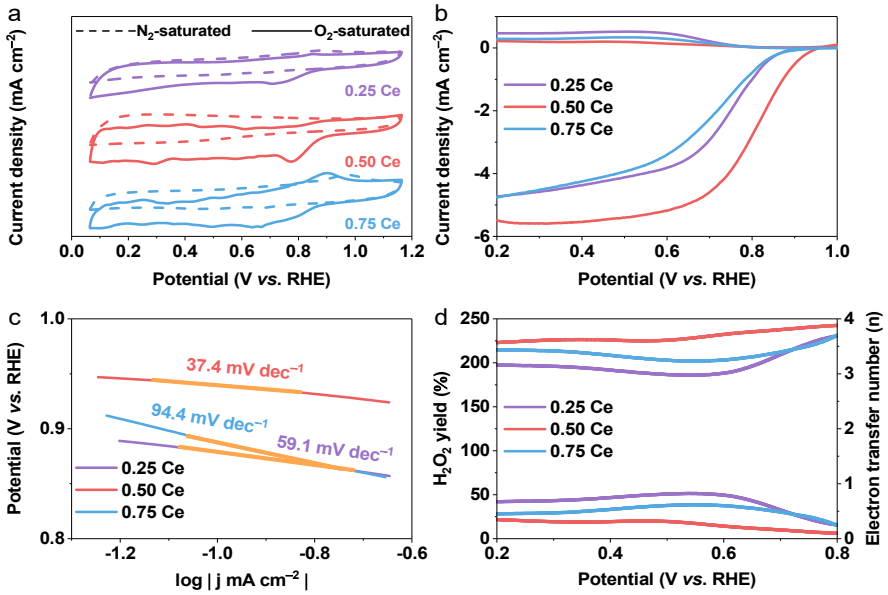

Fig. S10. (a) CV curves, (b) LSV polarization curves, (c) Tafel plots, and (d) H_2O_2 yield (%) and transfer electron number (*n*) for MnO-CeO_2@Cs with different Ce molar contents.

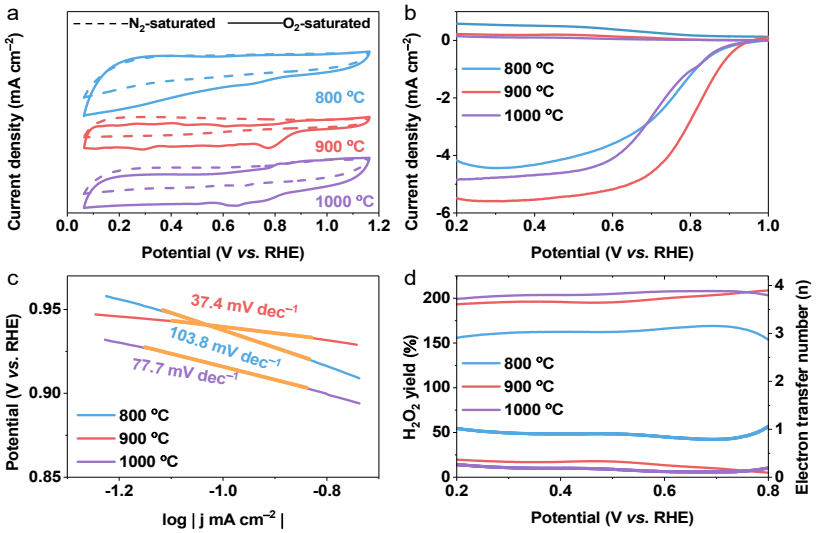

Fig. S11. (a) CV curves, (b) LSV polarization curves, (c) Tafel plots, and (d) H_2O_2 yield (%) and transfer electron number (n) for MnO-CeO_2@Cs at different calcination temperatures.

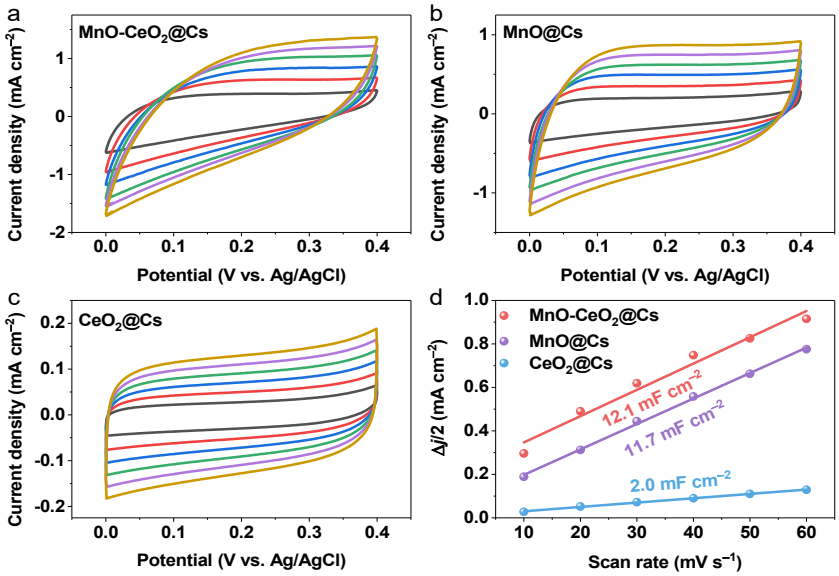

Fig. S12. CV curves of (a) MnO-CeO_2@Cs, (b) MnO@Cs, (c) CeO_2@Cs, and (d) MnO-CeO_2@Cs. (d) C_{dl} values of MnO-CeO_2@Cs, MnO@Cs, and (c) CeO_2@Cs.

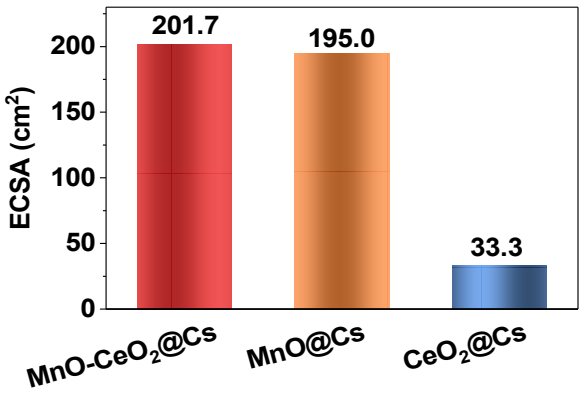

Fig. S13. Corresponding ECSA for MnO-CeO_2@Cs, MnO@Cs, and CeO_2@Cs.

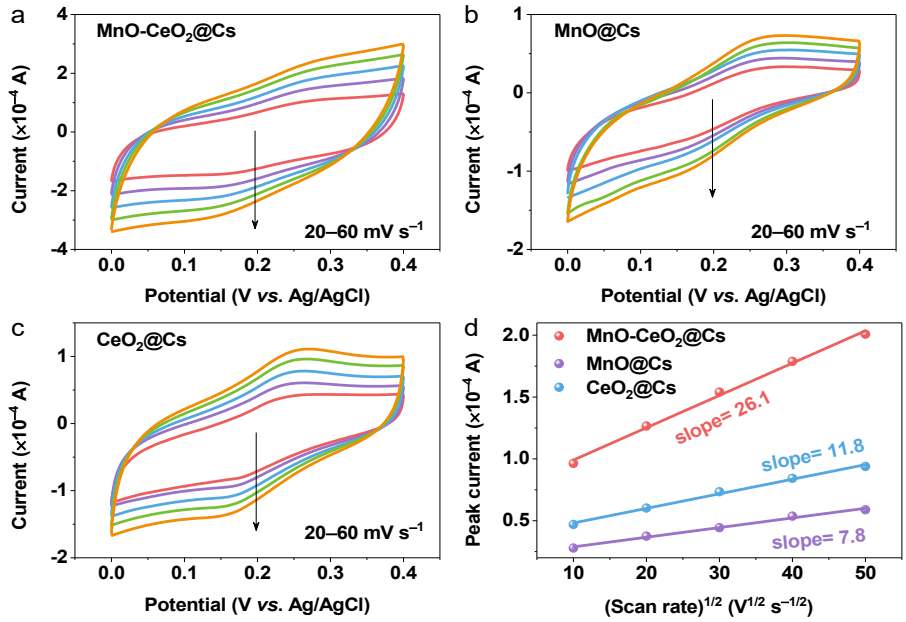

Fig. S14. CV curves of (a) MnO-CeO_2@Cs, (b) MnO@Cs, (c) CeO_2@Cs, and (d) MnO-CeO_2@Cs. (d) C_{dl} values of MnO-CeO_2@Cs, MnO@C, and CeO_2@Cs.

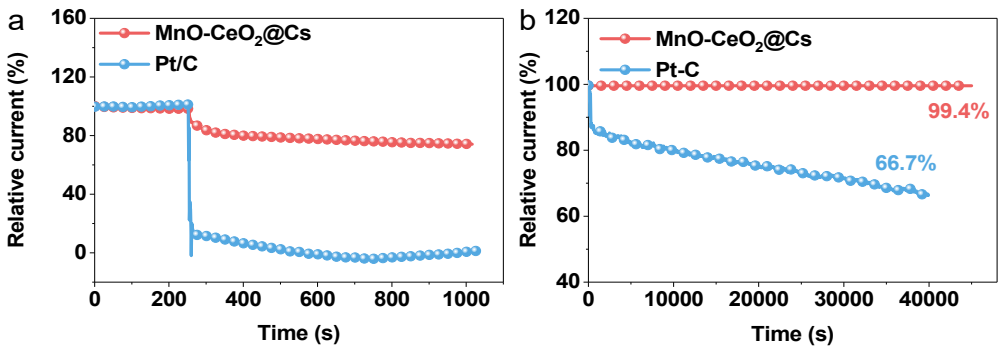

Fig. S15. (a) Methanol tolerance test of MnO-CeO_2@Cs and Pt/C (20 wt%) in O_2-saturated 0.1 M KOH solution with the addition of 3 M methanol at around 280 s, and (b) stability test of MnO-CeO_2@Cs and Pt/C (20 wt%) in O_2-saturated 0.1 M KOH solution at a rotating speed of 1600 rpm.

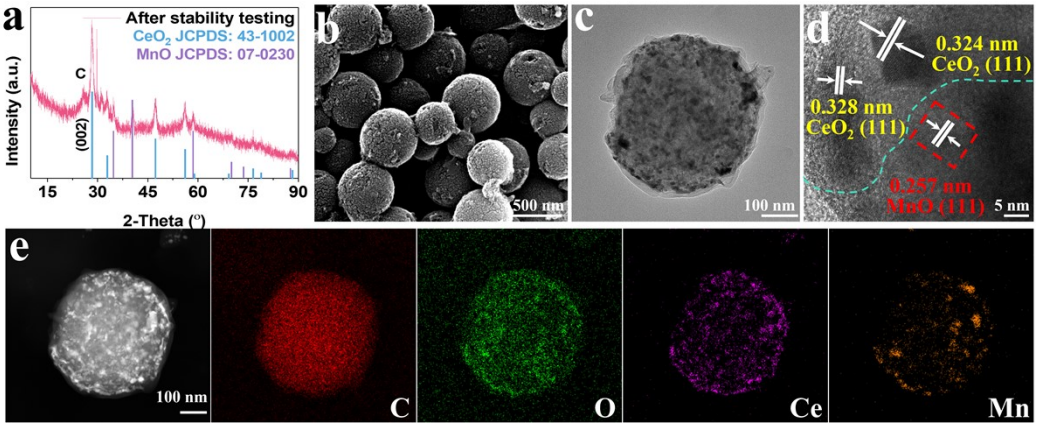

Fig. S16. Characterization after stability testing of MnO-CeO_2@Cs. (a) XRD pattern, (b) SEM image, (c) TEM image, (d) HR-TEM image, and (e) HAADF-STEM image and corresponding element mappings.

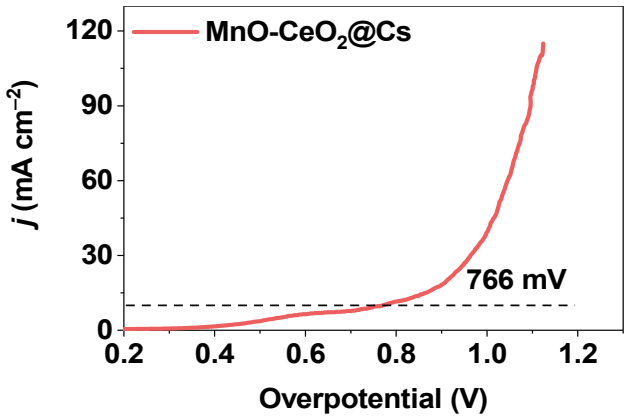

Fig. S17. LSV polarization curve of MnO-CeO_2@Cs.

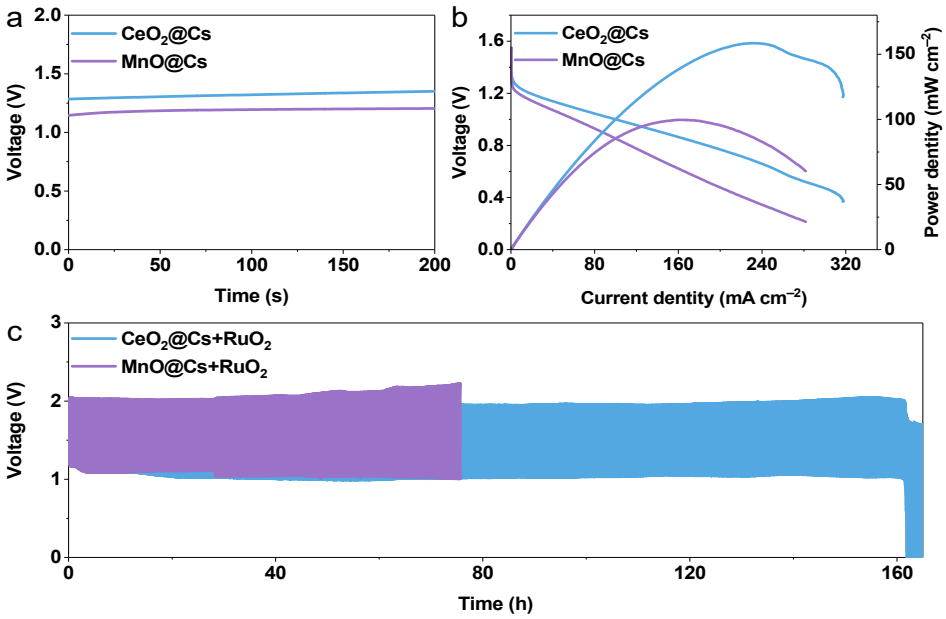

Fig. S18. (a) Open-circuit voltage (OCV) plots, and (b) discharge polarization curves and the corresponding power densities. (c) Galvanostatic cycling at 5 mA cm^{-2} (20 min for each cycle) of CeO_2@Cs and MnO@Cs-based aqueous ZABs.

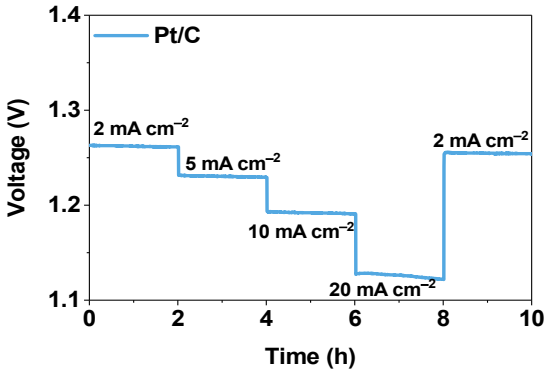

Fig. S19. Discharge profiles at various current densities of Pt/C.

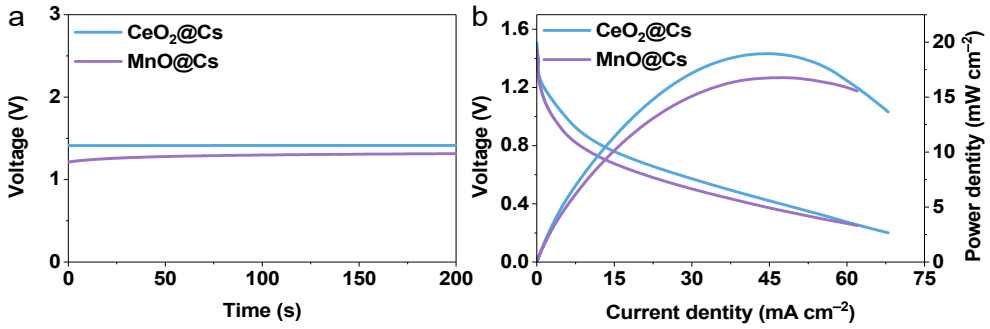

Fig. S20. (a) Open-circuit voltage (OCV) plots, and (b) discharge polarization curves and the corresponding power densities of CeO_2@Cs and MnO@Cs-based flexible ZABs.

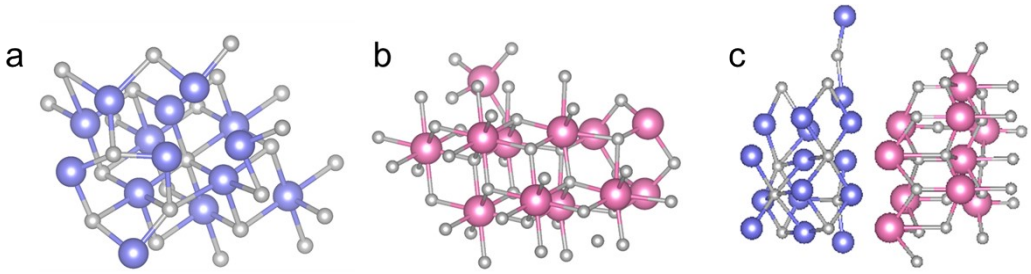

Fig. S21. Optimized structures of (a) MnO, (b) CeO_2, and (c) MnO-CeO_2.

Table S1. The ORR activity of different catalysts in 0.1 M KOH.

Sample	$E_{1/2}$ (V vs. RHE)	E_{onset} (V vs. RHE)
MnO-0.25CeO_2@Cs	0.73	0.89
MnO-0.50CeO_2@Cs	0.80	0.93
MnO-0.75CeO_2@Cs	0.68	0.89
MnO-CeO_2@Cs-800 ℃	0.74	0.92
MnO-CeO_2@Cs-1000 ℃	0.71	0.92
MnO@Cs	0.67	0.82
CeO_2@Cs	0.70	0.82

Table S2. Comparison of MnO-CeO_2@Cs with previously reported for ORR electrocatalysts in 0.1 M KOH solution.

Catalysts	$E_{1/2}$ (V vs. RHE)	E_{onset} (V vs. RHE)	Reference
MnO-CeO_2@Cs	**0.80**	**0.93**	**This work**
Ni–MnO/rGO	0.78	0.94	[6]
CMNC-1	0.84	0.97	[7]
MnO/Co/PGC	0.78	0.95	[8]
MnO@CNT@Co–N/C	0.81	0.93	[9]
MnOOH@CeO_2	0.80	0.90	[10]
CoO_x/CeO_2/RGO	0.83	0.88	[11]

Table S3. Comparison of ZAB performance between MnO-CeO_2@Cs and recently reported catalysts in the literature.

Catalysts	Power density (mW cm^{-2})	Specific capacity ($mA\ h\ g_{Zn}^{-1}$)	Reference
MnO-CeO_2@Cs	**200**	**806**	**This work**
Co_3O_4@$LaCoO_3$	140	785	[12]
CoP/CoO@MNC-CNT	152.8	724.6	[13]
Co_3O_4-S/NSG	150.1	738.1	[14]
Ni_3FeN/MnO-CNTs	197	700	[15]
Co/MnO@NC	148	768	[16]
CoN/Co_3O_4 HNPs@NCNWs	118.3	779.8	[17]
Co@Co_3O_4/PNC	158.5	781.8	[18]
Fe_3O_4/CoO@CF	137	740	[19]
3DOM Fe/Co@NC-WO_{2-x}	165.1	756	[20]

Table S4. Comparison of MnO-CeO_2@Cs with previously reported for flexible Zn-air batteries.

Catalysts	Peak power density (mW cm^{-2})	Reference
MnO-CeO_2@Cs	**67.0**	**This work**
Ru/HfO_2-NC	11.2	[21]
NF/CCO/FCH	35.2	[22]
CNF-FZAB-PF	30.0	[23]
$Co_{0.68}Fe_{0.32}O$@NC/CC	52	[24]
S–LDH/NG	86	[25]
Co/N@CNTs@CNMF-800	26.5	[26]
N-$NiSe_2$/CC	29	[27]
CoCu/N-CNS-2	77.6	[28]
Ru-RuO_2@NPC	29	[29]

References

1. K. Yuan, D. Lützenkirchen-Hecht, L. Li, L. Shuai, Y. Li, R. Cao, M. Qiu, X. Zhuang, M. K. H. Leung, Y. Chen and U. Scherf, *J. Am. Chem. Soc.*, 2020, **142**, 2404-2412.
2. G. Kresse and J. Furthmüller, *Phys. Rev. B*, 1996, **54**, 11169-11186.
3. G. Kresse and J. Furthmüller, *Comp. Mater. Sci.*, 1996, **6**, 15-50.
4. J. P. Perdew, K. Burke and M. Ernzerhof, *Phys. Rev. Lett.*, 1996, **77**, 3865-3868.
5. P. E. Blöchl, *Phys. Rev. B*, 1994, **50**, 17953-17979.
6. G. Fu, X. Yan, Y. Chen, L. Xu, D. Sun, J.-M. Lee and Y. Tang, *Adv. Mater.*, 2018, **30**, 1704609.

7. K. Li, R. Cheng, Q. Xue, T. Zhao, F. Wang and C. Fu, *ACS Appl. Mater. Interfaces*, 2023, **15**, 9150-9159.
8. X. F. Lu, Y. Chen, S. Wang, S. Gao and X. W. Lou, *Adv. Mater.*, 2019, **31**, 1902339.
9. F. Li, T. Qin, Y. Sun, R. Jiang, J. Yuan, X. Liu and A. P. O'Mullane, *J. Mater. Chem. A*, 2021, **9**, 22533-22543.
10. D. Liu, J. Tian, Y. Tang, J. Li, S. a. Wu, S. Yi, X. Huang, D. Sun and H. Wang, *Chem. Eng. J.*, 2021, **406**, 126772.
11. H. Zhong, L. Alberto Estudillo-Wong, Y. Gao, Y. Feng and N. Alonso-Vante, *J. Energy Chem.*, 2021, **59**, 615-625.
12. J. Ran, J.-F. Wu, Y. Hu, M. Shakouri, B. Xia and D. Gao, *J. Mater. Chem. A*, 2022, **10**, 1506-1513.
13. H. W. Go, T. T. Nguyen, Q. P. Ngo, R. Chu, N. H. Kim and J. H. Lee, *Small*, 2023, **19**, 2206341.
14. L. Meng, W. Liu, Y. Lu, Z. Liang, T. He, J. Li, H. Nan, S. Luo and J. Yu, *J. Energy Chem.*, 2023, **81**, 633-641.
15. Q. Lu, X. Zou, Y. Bu, K. Liao, W. Zhou and Z. Shao, *Small*, 2022, **18**, 2105604.
16. Y. Niu, X. Teng, S. Gong, X. Liu, M. Xu and Z. Chen, *Energy Storage Mater.*, 2021, **43**, 42-52.
17. Q. Zhou, S. Zhang, G. Zhou, H. Pang, M. Zhang, L. Xu, K. Sun, Y. Tang and K. Huang, *Small*, **19**, 2301324.
18. W. Wu, R. chen, S. Chen, Z. Wang and N. Cheng, *Small*, 2023, **19**, 2300621.
19. X. Li, Y. Liu, H. Xu, Y. Zhou, X. Chen, Z. An, Y. Chen and P. Chen, *J. Colloid Interface Sci.*, 2023, **640**, 549-557.
20. Q. Han, X. Zhao, Y. Luo, L. Wu, S. Sun, J. Li, Y. Wang, G. Liu and Z. Chen, *Adv. Sci.*, 2022, **9**, 2104237.
21. C. Hu, F. Wei, Q. Liang, Q. Peng, Y. Yang, T. Taylor Isimjan and X. Yang, *J. Energy Chem.*, 2023, **80**, 247-255.
22. X. Yang, Z. Zhou, Y. Zou, J. Kuang, D. Ye, S. Zhang, Q. Gao, S. Yang, X. Cai and Y. Fang, *Appl. Catal. B: Environ.*, 2023, **325**, 122332.
23. J. Wang, Y. Zhang, X. Guo, S. Liao, P. Lv and Q. Wei, *Nanoscale*, 2023, **15**, 625-630.
24. Y. Chong, Z. Pan, M. Su, X. Yang, D. Ye and Y. Qiu, *Electrochim. Acta*, 2020, **363**, 137264.
25. X. Han, N. Li, J. S. Baik, P. Xiong, Y. Kang, Q. Dou, Q. Liu, J. Y. Lee, C. S. Kim and H. S. Park, *Adv. Funct. Mater.*, 2023, **33**, 2212233.
26. T. Liu, J. Mou, Z. Wu, C. Lv, J. Huang and M. Liu, *Adv. Funct. Mater.*, 2020, **30**, 2003407.
27. S. Han, Y. Hao, Z. Guo, D. Yu, H. Huang, F. Hu, L. Li, H.-Y. Chen and S. Peng, *Chem. Eng. J.*, 2020, **401**, 126088.
28. J. Kuang, Y. Shen, Y. Zhang, J. Yao, J. Du, S. Yang, S. Zhang, Y. Fang and X. Cai, *Small*, 2023, **19**, 2207413.
29. N. Wang, S. Ning, X. Yu, D. Chen, Z. Li, J. Xu, H. Meng, D. Zhao, L. Li, Q. Liu, B. Lu and S. Chen, *Appl. Catal. B: Environ.*, 2022, **302**, 120838.